

Estimate of the Background and Sensitivity of the Follow-up X-ray Telescope onboard Einstein Probe

Juan Zhang^{a,*}, Liqiang Qi^a, Yanji Yang^a, Juan Wang^a, Yuan Liu^b, Weiwei Cui^a, Donghua Zhao^b, Shumei Jia^a, Tianming Li^{a,c}, Tianxiang Chen^a, Gang Li^a, Xiaofan Zhao^a, Yong Chen^a, Huaqiu Liu^d, Congying Bao^b, Ju Guan^a, Liming Song^a, Weimin Yuan^b

^a*Key Laboratory of Particle Astrophysics, Institute of High Energy Physics, Chinese Academy of Sciences, Beijing, 100049, China*

^b*National Astronomical Observatories, Chinese Academy of Sciences, Beijing, 100012, China*

^c*University of Chinese Academy of Sciences, Chinese Academy of Sciences, Beijing, 100049, China*

^d*Innovation Academy for Microsatellites, Chinese Academy of Sciences, Shanghai, 201210, China*

Abstract

As a space X-ray imaging mission dedicated to time-domain astrophysics, the Einstein Probe (EP) carries two kinds of scientific payloads, the wide-field X-ray telescope (WXT) and the follow-up X-ray telescope (FXT). FXT utilizes Wolter-I type mirrors and the pn-CCD detectors. In this work, we investigate the in-orbit background of FXT based on Geant4 simulation. The impact of various space components present in the EP orbital environment are considered, such as the cosmic photon background, cosmic ray primary and secondary particles (e.g. protons, electrons and positrons), albedo gamma rays, and the low-energy protons near the geomagnetic equator. The obtained instrumental background at 0.5-10 keV, which is mainly induced by cosmic ray protons and cosmic photon background, corresponds to a level of $\sim 3.1 \times 10^{-2}$ counts s^{-1} keV $^{-1}$ in the imaging area of the focal plane detector (FPD), i.e. 3.7×10^{-3} counts s^{-1} keV $^{-1}$ cm $^{-2}$ after normalization. Compared with the instrumental background, the field of view (FOV) background, which is induced by cosmic photons reflected by the optical mirror, dominates below 2 keV.

*Corresponding author

Email address: zhangjuan@ihep.ac.cn (Juan Zhang)

Based on the simulated background level within the focal spot (a $30''$ -radius circle), the sensitivity of FXT is calculated, which could theoretically achieve several μcrab (in the order of $10^{-14} \text{ erg cm}^{-2} \text{ s}^{-1}$) in 0.5-2 keV and several tens of μcrab (in the order of $10^{-13} \text{ erg cm}^{-2} \text{ s}^{-1}$) in 2-10 keV for a pointed observation with an exposure of 25 minutes. This sensitivity becomes worse by a factor of ~ 2 if additional 10% systematic uncertainty of the background subtraction is included.

Keywords: EP/FXT, space environment, Geant4 simulation, background, sensitivity

PACS: 0000, 1111

2000 MSC: 0000, 1111

1. Introduction

The Einstein Probe (EP) is a space X-ray astronomical mission led by the Chinese Academy of Sciences (CAS) in collaboration with the European Space Agency (ESA) and the Max-Planck-Institute for extraterrestrial Physics (MPE), Germany. It is scheduled to be launched into a low-Earth orbit (LEO) with an altitude of ~ 600 km and an inclination of 29° by the end of 2022. It is dedicated to time-domain astrophysics with primary goals to discover cosmic high-energy transients and monitor variable objects [1, 2, 3]. EP carries two kinds of scientific payloads, the Wide-field X-ray Telescope (WXT, 0.5-4 keV) and the Follow-up X-ray Telescope (FXT, 0.3-10 keV). WXT will be used to capture transients and to monitor variable objects, whereas FXT will be used to conduct deep follow-up observations of interesting targets discovered by WXT as well as by other facilities. WXT is equipped with the micro-pore lobster-eye optics, which achieves a large instantaneous field-of-view (FOV), 3600 square degrees (~ 1.1 sr), and a high sensitivity that is at least one order of magnitude better than those of the coded mask telescopes and pinhole/slit cameras currently in orbits, such as Swift/BAT and MAXI [4]. FXT uses Wolter-I optics with a focal length of 1.6 m and the pn-CCD based focal plane detector (FPD) with pixel size of $75 \mu\text{m} \times 75 \mu\text{m}$ [3].

To estimate the in-orbit background of detectors of space instruments before launch is an essential part of any X-ray mission development. On the one hand, these studies can be used not only to optimize the instrument design and to evaluate the onboard storage requirements, but also to

investigate whether the instrument could fulfill the scientific goals. On the other hand, the estimated background helps scientists to understand the performance of the telescope and conduct the pre-study of target sources of interest, and helps the mission operation team to draw up observation strategies. Each space instrument needs to conduct its own background estimation due to the different detector type and operation environment for different orbits, e.g. Tenzer et al. [5], Perinati et al. [6] and Weidenspointner et al. [7] for eROSITA, Fioretti et al. [8] for ATHENA, Campana et al. [9] for LOFT/LAD, Xie and Pearce [10] for Sphinx, Xie et al. [11] and Zhang et al. [12] for Insight-HXMT, and Zhao et al. [4] for a micro-pore lobster-eye telescope which is the prototype of EP/WXT.

In this work, we investigate the background and sensitivity of FXT. A method to estimate the in-orbit background of space instrument is to use Monte Carlo simulations facilitated by the Geant4 toolkit [13, 14, 15], which was developed for simulation of particle physics experiments. Geant4 could depict the interaction of particles with matter as realistically as possible. Different with what done for Insight-HXMT [11, 12], the simulation of FXT needs the process that describes the reflection of photons incident on the Wolter-I mirror with grazing angles. Currently Geant4 lacks these processes in its release versions. Fortunately, extended packages have been developed that could be incorporated into Geant4, e.g. the generic ray-tracing extension XRTG4 developed by Buis and Vacanti [16] and the physics model for the interaction of X-rays and matter at grazing incidences developed by Qi et al. [17]. For the proton scattering at grazing incidence angles off X-ray mirrors, the analytical model and semi-empirical model (e.g. [18, 19]) and Geant4 packages (e.g. [17, 20] and references therein) have been developed. In this work, the background simulation of FXT is conducted with Geant4 and the external packages developed by Qi et al. [17]. The mass modeling of FXT is established, including EP platform, WXT and FXT. The space radiation components in EP orbit environment are widely investigated. Based on the simulated background, the sensitivity of FXT is investigated.

2. EP/FXT

Figure 1 shows the latest configuration of EP. It consists of two scientific payloads, WXT and FXT. WXT is equipped with lobster-eye optics and has 12 identical modules forming a total FOV of 3600 square degrees (~ 1.1 sr), which makes it have excellent grasp capability [3] and ideal for the whole sky

monitoring of X-rays. FXT, as the follow-up observation telescope, utilizes Wolter-I mirrors and pn-CCD detectors forming a circular FOV with a diameter of ~ 1 degree (3×10^3 arcmin²). Compared to WXT, FXT has much larger effective area and angular resolution [1, 2, 3]. FXT comprises two co-aligned identical modules, surrounded by the 12 modules of WXT. The development of FXT is a collaboration among the CAS, ESA and MPE. The Institute of High Energy Physics (IHEP), CAS is responsible for the overall design, development and test of the entire FXT instrument, while ESA and MPE contribute to the FXT development via provision of some of the key components of FXT including the mirror assemblies, use of the mirror design and mandrels, electron diverter, and CCD detector modules¹.

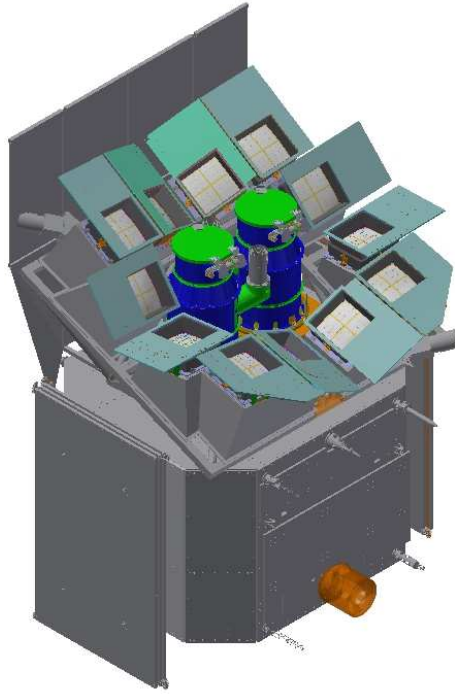


Figure 1: The latest configuration of EP. The two blue tubes in the center are the two FXT modules. Surrounded are the 12 modules of WXT.

¹ESA provides one set of the Mirror Assembly and the Electron Diverter, and MPE provides the eROSITA design information and use of the mandrels, one eROSITA Mirror Flight Spare and Mirror Demonstrator Model, and a number of detector modules plus CAMEX test module.

The optics of FXT is similar to that of the eROSITA telescopes, which consists of 54 Wolter-I type mirror shells, with an outer diameter of ~ 36 cm on the top and 7.6 cm at the bottom and a focal length of 1.6 m. For each shell, a layer of 100 nm thick gold is coated on the nickel substrate. The FPD of FXT is the pn-CCD. The sensitive layer of the pn-CCD is $450 \mu\text{m}$ silicon, which is covered by 20 nm SiO_2 , 30 nm Si_3N_4 and an on-chip filter of 90 nm aluminum, as illustrated in Figure 2. The FPD has an imaging area and a frame-store area. There are 384×384 pixels in the imaging area, each pixel with a size of $75 \mu\text{m} \times 75 \mu\text{m}$. The frame-store area also has 384×384 pixels correspondingly, but with smaller pixel size, $51 \mu\text{m} \times 75 \mu\text{m}$. The FPDs of the two FXT modules are placed by rotating an angle of 90 degree relative to each other in the focal plane of FXT so that they could be complementary to each other during observation. The pn-CCD is placed inside an aluminum alloy detector box, which is nested into a ~ 3 cm thick copper box, in order to shield the cosmic ray particles and photon background in the space environment outside the FOV of FXT.

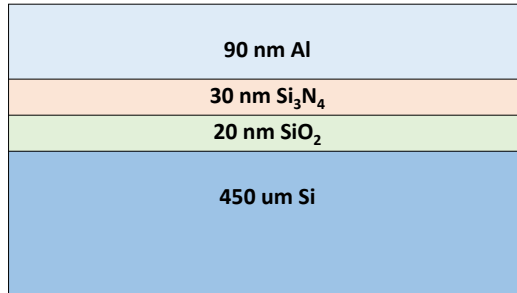


Figure 2: On-chip filters above the pn-CCD.

In addition to the on-chip filter, there is also a filter wheel between the Wolter-I optics and the FPD inside each FXT module. There are six positions on the filter wheel, as illustrated in Figure 3. The closed position is filled with a 2 mm aluminum and is used to obtain the instrumental background during the in-orbit observation. The thin, medium and thick filters, which are different in the thickness of the aluminum (Al) and the polyimide (PI), are used to observe sources with different fluxes to avoid the pile-up effect. The other two positions, not shown in this figure, are the open setup and the in-orbit calibration source setup.

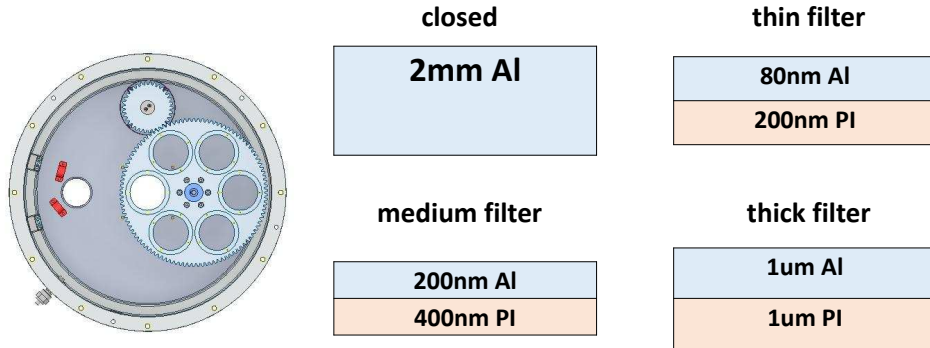


Figure 3: The filter wheel of FXT.

3. Space environment

EP will be launched into a circular LEO with an altitude of 600 km and an inclination of 29° by the end of 2022. In such an orbit, there are various space radiation components that may cause background events in FXT, such as the cosmic photon background, the cosmic rays (primary and secondary protons, electrons, and positrons, etc.), the low energy charged particles which are enhanced near the geomagnetic equator, and the albedo gamma rays. In this section, we describe these space radiation components and the models we adopt for the background simulation of FXT.

3.1. Cosmic photon background

The cosmic photon background includes emissions from the unresolved sources outside our Galaxy, i.e. the cosmic X-ray background (CXB), and the diffuse Galactic foreground. Generally CXB is modeled by a broken power-law [21, 22] from keV to several hundred of MeV. These models have been used in the simulation of LOFT/LAD [9] and Insight-HXMT [11, 12]. For the diffuse Galactic foreground, the contributed photons are softer. McCammon et al. have given a high spectral resolution observation of the soft x-ray diffuse background, of which the spectrum could be fitted by a two-temperature thermal plus power-law model [23]. This model is denoted by `apec+wabs(apec+const*powerlaw)` in XSPEC and has been used for the background simulation of Athena/WFI[24]. The parameters are listed in Table 1. The `powerlaw` term, `wabs*const*powerlaw`, represents the extragalactic diffuse emission from unresolved sources. The two-temperature thermal term, `apec+wabs*apec`, models the diffuse Galactic foreground.

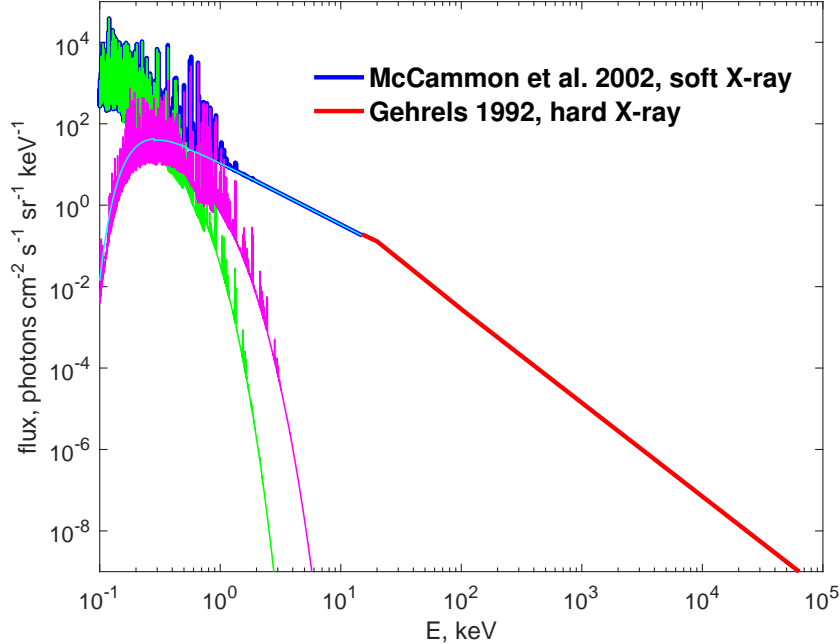


Figure 4: The cosmic photon background spectra used in the FXT background simulation. The CXB spectrum [21] above 15 keV is plotted in red, and labeled with “Gehrels 1992, hard X-ray”. The high resolution soft X-ray spectrum [23] is denoted by “McCammon et al. 2002, soft X-ray”. Also plotted are the three components of the soft spectrum. The two temperature equilibrium thermal emission with and without absorption are in magenta and green respectively. The absorbed power-law spectrum with an constant factor of 1 is plotted in cyan.

Given the energy band of interest of FXT, 0.3-10 keV, in this work the soft X-ray diffuse background spectrum [23, 24] is used for photons with energy less than 15 keV and the CXB spectrum [21] is adopted above 15 keV, as shown in Figure 4. Note that the constant factor of the power-law component of the soft X-ray spectrum model is taken as 1 for the background simulation of FXT instead of a value of 0.2 used for Athena/WFI. This is because the goal sensitivity of Athena/WFI is much better, $\sim 10^{-17}$ erg cm $^{-2}$ s $^{-1}$ for a 100 ks observation². With such a good sensitivity, it is assumed that 80% of the pointed sources could be resolved from CXB. Therefore a factor of 0.2

²<https://tuprints.ulb.tu-darmstadt.de/2980/>

is used for Athena/WFI [24]. While for EP/FXT, the typical pointing observational exposure is 1500 seconds according to the planned observational strategy. It doesn't have good enough sensitivity to resolve point sources from CXB. Thus a factor of 1 is used. The CXB spectrum adopted from [21] is presented in Equation 1.

$$F = \begin{cases} 0.54 \times E^{-1.4}, & E < 0.02 \text{ MeV} \\ 0.0117 \times E^{-2.38}, & 0.02 \text{ MeV} < E < 0.1 \text{ MeV} \\ 0.014 \times E^{-2.3}, & E > 0.1 \text{ MeV} \end{cases} \quad (1)$$

where E is in MeV and F in photons $\text{cm}^{-2} \text{s}^{-1} \text{MeV}^{-1} \text{sr}^{-1}$. At first during the simulation, we ignore the spacial anisotropy of the cosmic photon background and take it to be uniformly distributed in the whole sky. This may be not suitable for soft X-rays diffuse background due to its change with different Galactic pointing directions. In the following sections, the impact of this change and its impact on the background and sensitivity will be discussed.

Table 1: Model parameters for the soft X-ray diffuse background, which is expressed by wabs(apec+const*powerlaw) using XSPEC notation. Normalizations are scaled to 1 arcmin². This table is adopted from [24]. The difference is that the constant factor of the power-law component is taken as 1 for the background simulation of FXT

Model	Parameter	Value
apec	kT ¹⁾	0.099
apec	abundance	1
apec	redshift	0
apec	norm ²⁾	1.7E-6
wabs	NH ³⁾	0.018
apec	kT ¹⁾	0.225
apec	abundance	1
apec	redshift	0
apec	norm	7.3E-7
const		1
powerlaw	photon index	1.52
powerlaw	norm	9.4E-7 ⁴⁾

¹⁾ kT is in keV

²⁾ in units of $10^{-14}/(4\pi D_A(1+z))^2 \int n_e n_H dV$, where D_A is the angular size distance to the source (cm), and n_e and n_H are the electron and H densities (cm⁻³)

³⁾ in units of 10²² cm⁻²

⁴⁾ in units of photons/keV/cm²/s @ 1 keV

3.2. Cosmic rays

Cosmic rays are high energy charged particles generated from outside the Earth. Generally, it is believed that cosmic rays above \sim EeV originate from outside the Galaxy, while those below this energy come from our Galaxy. For LEO satellites, the encountered cosmic rays are modulated by the solar activity and the geomagnetic fields, as described in Equation 2,

$$\begin{aligned}
 F(E) = F_{\text{LIS}}(E + |Z|e\Phi) \times \frac{(E + mc^2)^2 - (mc^2)^2}{(E + mc^2 + |Z|e\Phi)^2 - (mc^2)^2} \\
 \times \frac{1}{1 + (R/R_{\text{cut}})^{-r}}
 \end{aligned}
 \tag{2}$$

where E , m and Z are the kinetic energy, the rest mass and the charge of the cosmic ray particle, respectively. The first term, F_{LIS} , is the cosmic ray flux

of the local interstellar (LIS) environment. The second term depicts the solar modulation on F_{LIS} . It is described by the “force field approximation” model [25], where Φ is solar modulation potential, which varies from ~ 300 MV for solar activity minimum to ~ 1300 MV for solar activity maximum [26]. During the solar minimum, more low energy cosmic rays could enter the solar system. On the contrary, they will be shielded due to the higher potential during the solar maximum. The design lifetime of EP is 3 years, with a goal of 5 years. According to the predicted solar activity, as shown in Figure 5, the operation duration of EP is approaching to or around the solar maximum year.

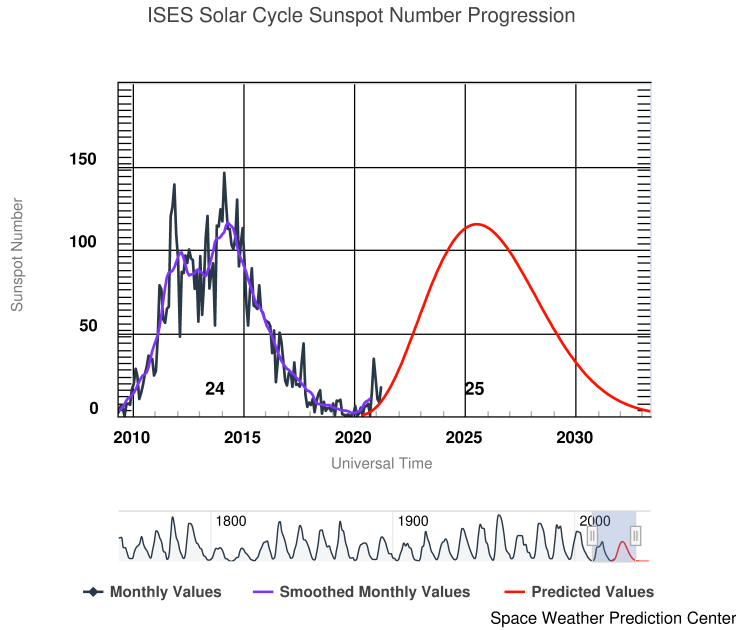


Figure 5: The predicted solar activity. This figure is adopted from <https://www.swpc.noaa.gov/products/solar-cycle-progression>

The third term of Equation 2 describes the modulation of the geomagnetic field, where $r = 12$ for protons, and $r = 6$ for electrons and positrons [27]. R is the particle rigidity, $R = pc/Ze$, where p is the momentum of this particle. R_{cut} is the cut off rigidity of a given location at the orbit of EP. This parameter represents the minimum energy needed by a primary cosmic ray particle to reach a given location at the Earth. It is related to the altitude and the geomagnetic latitude of this location and could be calculated by

assuming a dipole geomagnetic field [27],

$$R_{\text{cut}} = 14.9 \times \left(1 + \frac{h}{R_{\text{Earth}}}\right)^{-2} (\cos\theta_M)^4 \text{GV} \quad (3)$$

where R_{Earth} is the radius of the Earth, h the space altitude, and θ_M the geomagnetic latitude. For the EP orbit, with an altitude of 600 km and an inclination of 29 degree, θ_M varies from 0 to 0.7 rad ³. It can be seen that with the same altitude in the EP orbit, the high geomagnetic latitude 0.7 rad corresponds to a cut off rigidity of ~ 4.3 GV and the equatorial geomagnetic latitude corresponds to ~ 12.6 GV, which implies that there are more primary cosmic ray particles at several GeV around the high latitude of the geomagnetic field.

3.2.1. Primary protons

Protons are the dominant component among cosmic ray particles. The spectrum of primary cosmic ray protons has been precisely measured by AMS-01 [28, 29] and AMS-02 [30]. And the power-law spectral model based on measurements, $F_{\text{LIS}} = 23.9 \times \left[\frac{R(E)}{\text{GV}}\right]^{-2.83}$ particles $\text{m}^{-2} \text{s}^{-1} \text{sr}^{-1} \text{MeV}^{-1}$, was also widely used for the simulation of space instruments, e.g. [9, 27]. One can also obtain the orbital averaged spectrum of cosmic ray protons from ESA's SPace ENVironment Information System⁴ (SPENVIS, one can get the geographic and geomagnetic information of a spacecraft, the radiation environment and dose, etc. from SPENVIS). In this work, the spectrum from SPENVIS is used for the background simulation of FXT, as plotted in Figure 6. It is worth noting that this spectrum is also consistent with the spectrum obtained by averaging the AMS-01 measurements from 0 to 0.7 rad [28]. We show in Figure 6 the spectra resulting from the power-law model and including modulation by solar activity and the effect of geomagnetic latitude.

³<http://wdc.kugi.kyoto-u.ac.jp/igrf/gggm/index.html>

<https://omniweb.gsfc.nasa.gov/vitmo/cgm.html>

⁴<https://www.spnvis.oma.be>

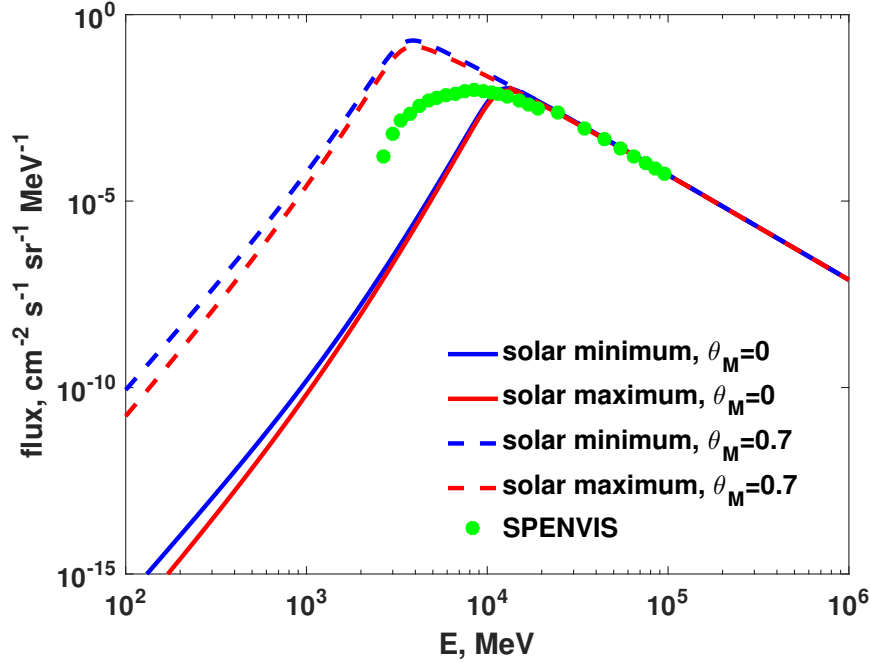


Figure 6: The spectra of primary cosmic ray protons in EP orbit. The blue and red lines denote the different solar activities, and the dashed and solid lines correspond to different geomagnetic latitudes. The spectrum shown as green dots are the average spectrum obtained from SPENVIS for the EP orbit.

3.2.2. Secondary Protons

Secondary cosmic ray particles are produced from the collisions of the primaries with the Earth's atmosphere. They are also strongly dependent on the geomagnetic field. Their spectra in different geomagnetic cutoff can be modeled by the broken power-law or the cutoff power-law model [27]. In this work, we use a spectrum obtained by averaging the AMS-01 measurements [28] between $\theta_M = 0 \sim 0.7$ rad to simulate the background induced by secondary protons. This spectrum is shown in Figure 7.

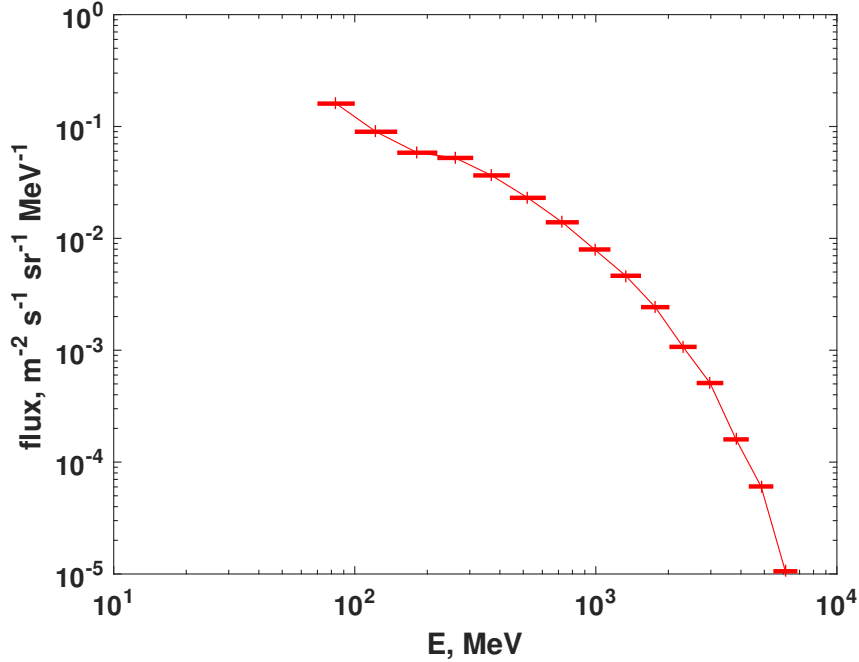


Figure 7: The incident spectral model of secondary protons used in EP orbit.

3.2.3. Low energy protons near the equator

Besides the primary and secondary cosmic ray protons, it was found that there are enhancements of proton flux with energies from tens keV to several MeV near the geomagnetic equator [31]. They are believed to be produced by the charge exchange between the inner radiation belt protons and the neutral atoms of the atmosphere, and the spectrum of these low energy protons can be modeled by a kappa function [32, 33],

$$f(E) = A \left[1 + \frac{E}{kE_0} \right]^{-k-1}, \quad (4)$$

where A is in $\text{cm}^{-2} \text{s}^{-1} \text{sr}^{-1} \text{keV}^{-1}$, E and E_0 in keV. $A=50$, $k=2.3$ and $E_0=30$ for the quiet geomagnetic conditions, and $A=330$, $k=3.2$ and $E_0=22$ for the disturbed conditions [33]. Though they are easily blocked by the shielding materials around the detector, these low energy protons have to be taken into account due to the funneling effects of the focusing mirrors [34, 35, 17, 36]. In our simulation, the kappa function with $A=328$, $k=3.2$ and $E_0=22$ [32] is used.

3.2.4. Primary electrons and positrons

The latest precise measurements of AMS-02 showed that the spectra of primary cosmic ray electrons and positrons have different magnitudes and energy dependences [37, 38]. Besides these newest measurements, a frequently used model of the LIS electrons is given by Mizuno et al. [27],

$$F_{\text{LIS}} = 0.65 \times \left[\frac{R(E)}{\text{GV}} \right]^{-3.3} \text{ counts m}^{-2} \text{ s}^{-1} \text{ sr}^{-1} \text{ MeV}^{-1} \quad (5)$$

where $R(E)$ is the rigidity of the electron. And the positron ratio, $e^+/(e^+ + e^-)$, is generally taken as 0.11 [39]. Figure 8 shows the modeled primary electrons and positron spectra for a solar minimum and a geomagnetic latitude of $\theta_M = 0.7$. Also shown are the primary cosmic ray electrons and positrons of AMS-02 [37, 38] after modulation by the geomagnetic field at $\theta_M = 0.7$. To obtain a conservative estimate of the background, the modeled spectra are used in this work.

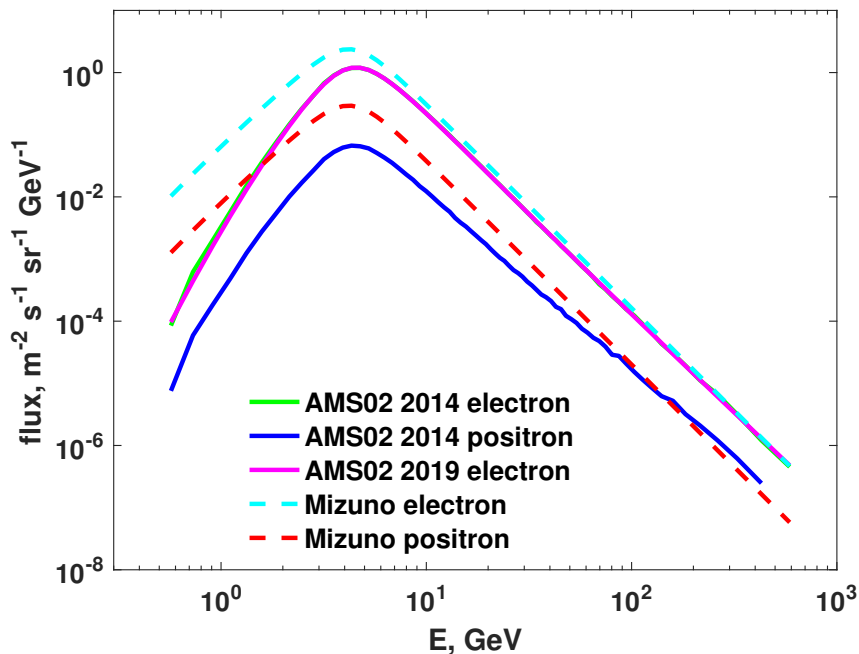


Figure 8: The spectra of primary cosmic ray electrons (dashed cyan) and positrons (dashed red) used for FXT simulation. Also plotted are the electron and positron spectrum of AMS-02 [37, 38] after the geomagnetic modulation at $\theta_M = 0.7$ in the EP orbit.

3.2.5. Secondary electrons and positrons

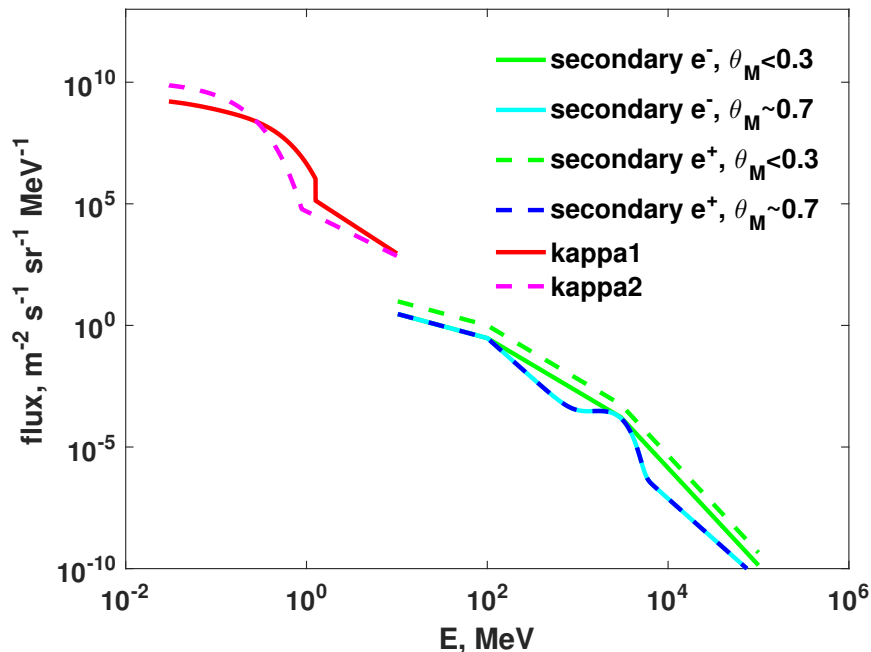


Figure 9: Secondary electron and positron spectra at different geomagnetic latitudes. The two spectra below 10 MeV are the enhanced electrons at $L < 2$ [40].

The spectra of secondary electrons and positrons can be modeled by the PL model, the broken power-law model or a power-law model with a hump model, which is correlated with the geomagnetic latitudes [27]. Different from the primary electrons and positrons, the positron/electron ratio varies with the geomagnetic latitude [27]. The secondary electron and positron spectra at regions of $0 \leq \theta_M \leq 0.3$ and $0.6 \leq \theta_M \leq 0.8$ are shown in Figure 9. For the simulation of FXT, we adopt the upper spectra corresponding to those at $0 \leq \theta_M \leq 0.3$.

In Figure 9 we show the spectra of low energy electrons from 10 keV to 10 MeV for the two flux-enhancement areas, i.e. the near-equatorial zone and the middle latitude zone [40]. For Wolter-I type X-ray telescopes, generally there is a magnetic deflector at the back end of the mirror to prevent low-energy charged particles from focusing on the FPD. In fact, low-energy electrons could be completely shielded with certain configurations of the mag-

netic deflector [36]. FXT is also equipped with the magnetic deflector. Therefore these low-energy electrons are not included in the following background simulation.

3.3. Albedo gamma rays

The albedo gamma rays originate from the interaction of the cosmic rays with the atmosphere and the atmosphere reflection of CXB. Therefore the albedo gamma ray flux strongly depends on the direction of the Earth relative to the instrument FOV. In this work, the spectrum of albedo gamma rays from Campana et al. [9] is adopted. According to the current observing strategy of EP⁵, most of the scientific observations are conducted around the zenith-pointing. Thus a zenith attitude of EP and an uniform distribution of the albedo gamma rays from the surface of the Earth are assumed for the simulation.

4. Geant4 mass modeling

The mass model of EP/FXT is built under the the framework of Geant4 Version 10.5.p1. In this section the detector construction, physics process, and generation of the incident particles are introduced.

4.1. Detector construction

Figure 10 shows the constructed structure of EP in Geant4. Figure 10 (a) illustrates the whole structure of EP. It consists of three parts, the platform, the WXT and the FXT. Most of the structure is constructed using the Constructive Solid Geometry (CSG) representations of Geant4. The platform is shown as the transparent yellow polygons at the bottom and it is built according to the realistic geometry dimensions and is filled by the aluminum with an equivalent density that is derived from its realistic mass. WXT is simplified as a hollow square around the two FXT modules. It is also assigned by the aluminum material with an equivalent density derived from its own weight. The FXT is constructed in more detail, as shown in Figure 10 (b). The 54 layers of Wolter-I mirror are built by using the paraboloid of Geant4 and the extension of hyperboloid developed by Qi et al. [17]. The imaging area of the pn-CCD is defined as the sensitive detector, and the deposited

⁵http://ep.nao.cas.cn/epmission/epoperation/201907/t20190724_505559.html

energy, position and time of each hit on this sensitive detector is output for further analysis.

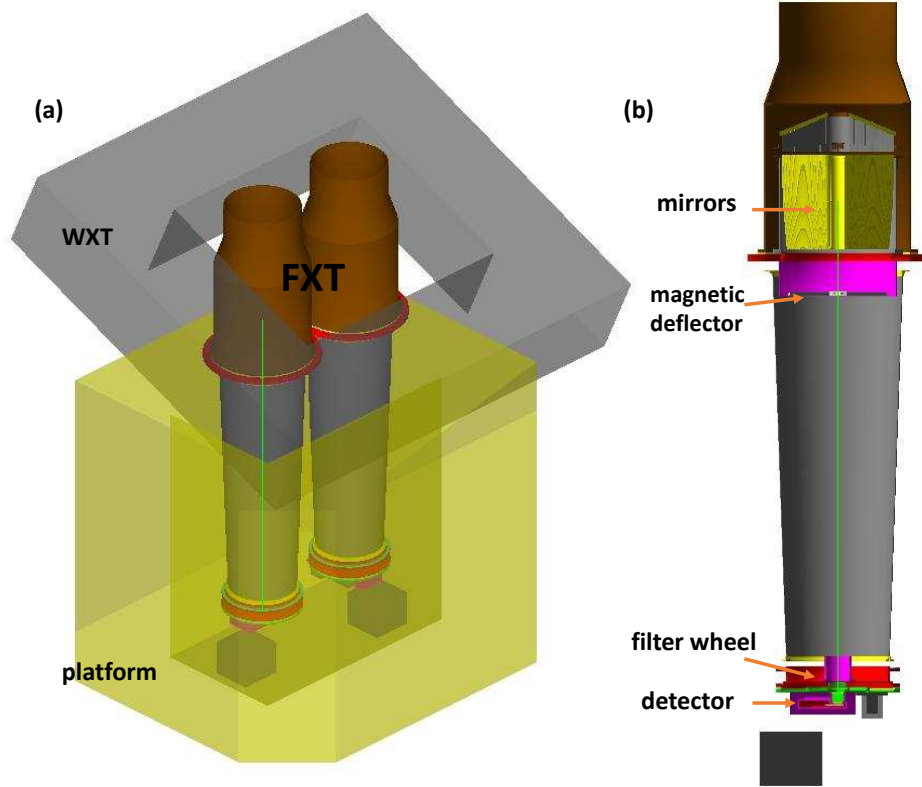


Figure 10: (a) The whole structure of EP constructed in the mass model of Geant4. (b) The cut-away view of the detailed FXT structure.

4.2. Physics

Given the energy range of interest of FXT and the energies and types of the incident particles in the EP orbit, the electromagnetic physics constructor G4EmStandardPhysics_option4 is chosen, which has an optimal mixture for the interaction precision. The options of fluorescence (Fluo), particle induced X-ray emission (PIXE) and auger processes are all set to be active. For the interaction of photons incident with grazing angles on the Wolter-I mirror, the physics model developed by Qi et al. [17] is used with a micro-roughness of 0.5 nm. And for the scattering of low-energy protons in the mirror, the single scattering model is used. For silicon detectors, the radioactive background is

generally not important and thus this process is not included in current simulation. These are detailed physical processes involved in the silicon-based detectors [41], e.g. the electron-hole pair production, the charge splitting and charge collections, which are not included in the simulation currently.

4.3. Primary Generation

Generally, the particle type, time, energy, position and direction are needed as the input parameters of the Geant4 simulation. The energy is easily obtained according to the spectral distribution of each background type as presented in Section 3. While considering the large structure of the EP satellite and the small sensitive geometry of FXT, $28.8\text{mm} \times 28.8\text{mm}$, to improve the simulation efficiency, a method for sampling the position and direction of incident particles is introduced. Figure 11 illustrates how the direction and position are sampled. Firstly, a circle with a diameter large enough to cover the cross section of EP is chosen, shown as the blue plane in Figure 11. Then a direction is chosen according to the direction distribution of each particle type. Finally the position is generated by putting this circle plane in that direction, and sampling uniformly on the circle plane.

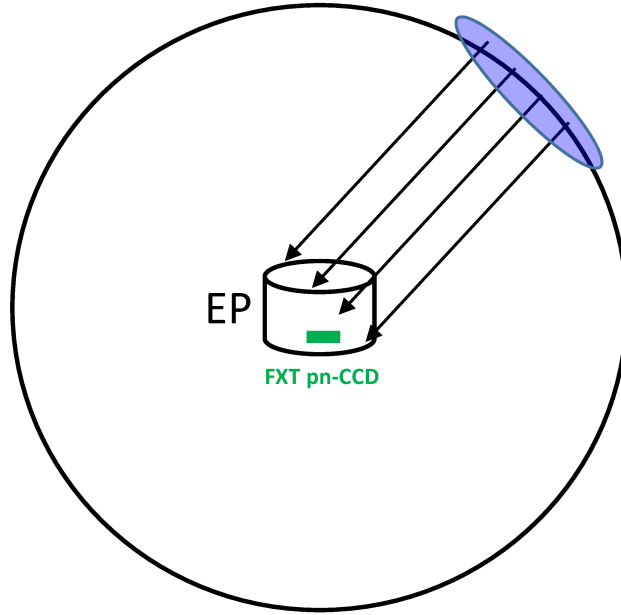


Figure 11: The direction and position generation in Geant4 mass modeling of EP/FXT.

5. Simulation Results

In this section, the background and sensitivity results of FXT are given. The hit information, i.e. the deposited energy, location, and time of each hit on the imaging area, output from Geant4 simulation are analyzed to obtain the background of FXT. Almost all hitting time of the responses of one incident event on the FPD are within the frame time of the pn-CCD. Though the charge splitting mode is not included in the simulation process, incident particles might also cause responses on more than one pixel (as illustrated in Figure 14 for the tracks caused by the cosmic ray protons). These background events are easily to be discarded. So the first step of the data analysis is to assign the hit information to the 384×384 pixels of the pn-CCD. The background events that deposit energy on more than three pixels are discarded. For the remaining events, their energies are obtained by adding up the deposited energy on all the hitting pixels. The positions of the background events are calculated by averaging the pixel center locations weighted by their deposited energies.

5.1. Background

The background contributions to the FPD of FXT are classified into two types, the FOV background and the instrumental background. The former one refers to the background caused by the focusing of the mirrors, such as the reflected cosmic photon background and the funneled low energy protons. The latter is induced by space particles that interact with the instrument and materials around the FPD and finally hit on the pn-CCD, e.g. the background induced by cosmic ray protons and electrons, by higher energy photons of the cosmic photon background and by albedo gamma rays, etc.

For the FOV background of cosmic photons, Figure 12 shows the distribution of the number of hit pixels, the tracks of some background events and the background event distribution on the FPD. The same plots for the background induced by equatorial low energy protons are also presented in Figure 13. It can be seen that all the FOV background events hit no more than four pixels and most of them hit only one pixel. Due to the focusing effect of the Wolter-I mirror, the distribution of the FOV background on the FPD are not uniform, and more concentrated towards the center of the FOV.

For the instrumental background, more pixels are impacted, and their distribution on the FPD is uniform, as shown in Figure 14 and Figure 15 for the instrumental background caused by primary cosmic ray protons and cosmic

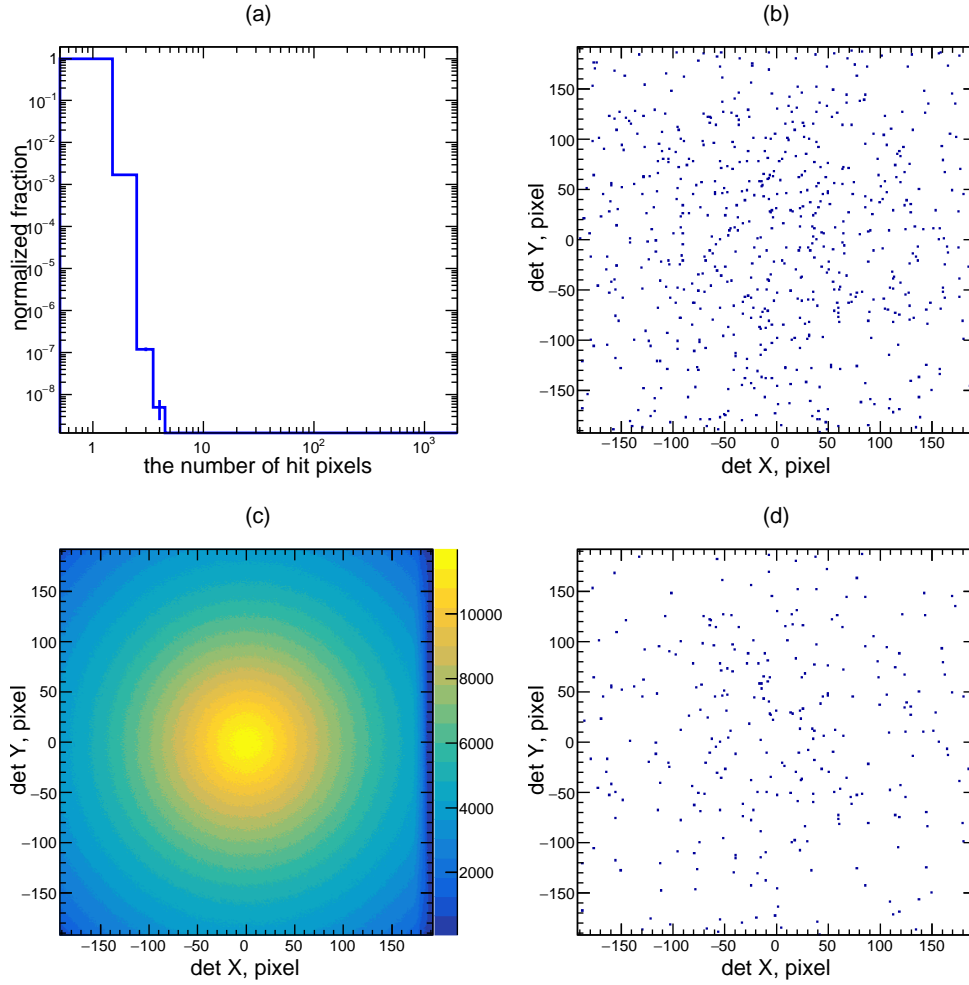


Figure 12: The characteristic of FOV background induced by cosmic photons. (a) The statistical distribution of the number of pixels that one background event deposits energy on; (b) Tracks of the background events without energy and pixel screening for an exposure of ~ 201 seconds; (c) The background event distribution on the imaging area after data screening and this distribution presents the vignetting effect of the Wolter-I mirror; (d) The same as panel (b) for background events after an energy (0.5-10 keV) and pixel (deposited pixel number < 4) screening.

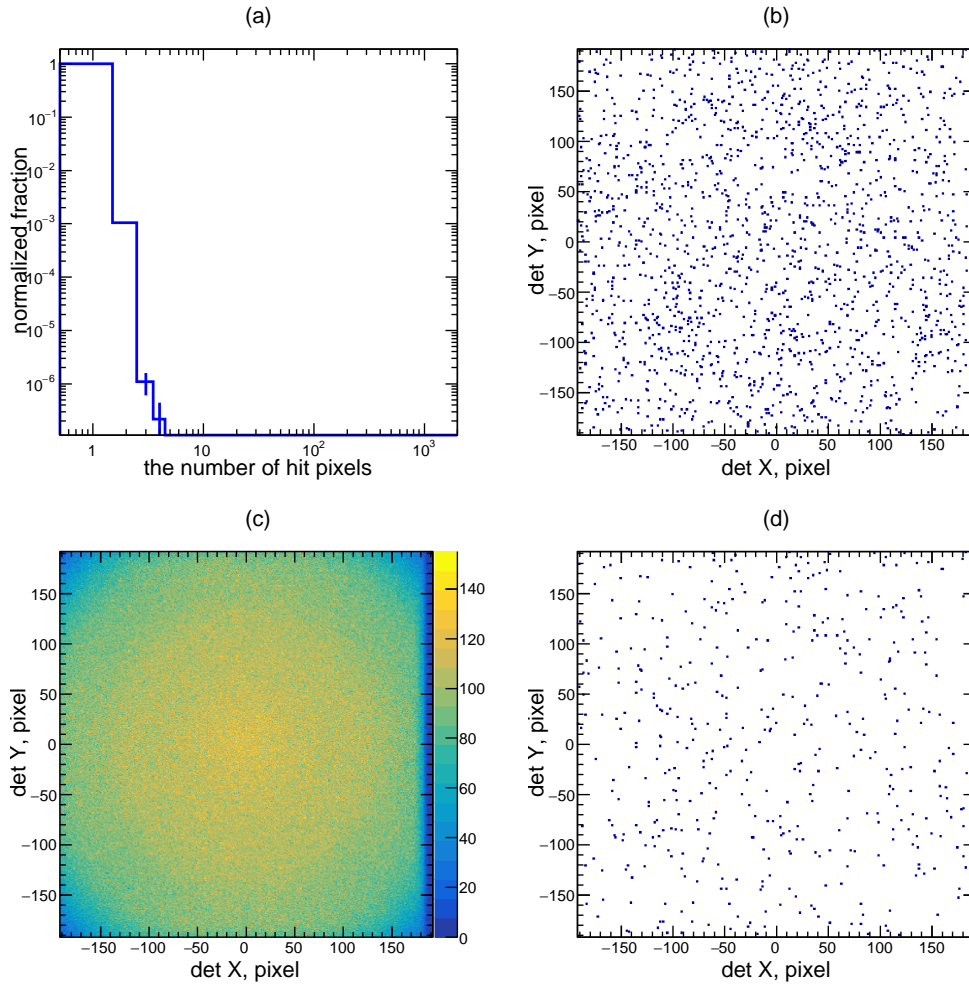


Figure 13: The characteristic of FOV background induced by equatorial low-energy protons. Each panel gives the same result as Figure 12, except that (b) is the tracks about 212 seconds.

photons, respectively. It is worth noting that the instrumental backgrounds are obtained by setting the filter wheel to the closed position in the Geant4 mass model. It can be seen from these figures that long tracks could be caused especially by the cosmic ray protons. About 16% background events of cosmic photons hit more than three pixels, while this value is 78% for primary cosmic ray protons.

Figure 16 gives the background spectra of various components on the imaging area of the FPD of FXT after getting rid of events that hit more than three pixels. The FOV background of the equatorial low energy protons (FOV low energy protons) are given corresponding to the open position of the filter wheel. It can be seen that the instantaneous background level of the equatorial low energy protons, $\sim 0.1 \text{ counts s}^{-1} \text{ keV}^{-1}$, is much higher than the instrumental background. However, these low energy protons only exist near the geomagnetic equator. On the one hand, the time intervals when these background events exist are easy to be thrown away through the selection of housekeeping data or the selection of the background rate above several keV. On the other hand, they are easily to be shielded by the materials of the filtered positions of the filter wheel. Therefore in the following text, the background and sensitivity results are all obtained by neglecting this background component.

The instrumental background spectra of primary cosmic ray protons (crp), primary cosmic ray electrons (cre-) and positrons (cre+), secondary cosmic ray protons (secondary protons), secondary cosmic ray electrons (secondary e-) and positrons (secondary e+), cosmic photon background (outside FOV), and albedo gamma rays (albedo gamma) have an almost flat shape among 0.2-12 keV. The most dominant instrumental background components are induced by primary cosmic ray protons and cosmic photon background. The Cu $K\alpha$ line at $\sim 8 \text{ keV}$ is obvious, which comes from the fluorescence line of the copper shielding box around the FPD. The line between 1.4-1.5 keV on the spectrum of cosmic ray protons comes from the aluminum of the closed position of the filter wheel [42]. The total instrumental background in the energy range from 0.5 to 10 keV on the whole imaging area of the FPD corresponds to a level of $\sim 3.1 \times 10^{-2} \text{ counts s}^{-1} \text{ keV}^{-1}$, i.e. $3.7 \times 10^{-3} \text{ counts s}^{-1} \text{ keV}^{-1} \text{ cm}^{-2}$ after area normalization.

The FOV background spectra of cosmic photons corresponding to the open position of the filter wheel (filter open), the thin filter position (the green line), the medium filter position (the blue line) and the thick filter position (the magenta line) are all present in Figure 16. Table 2 lists the FOV

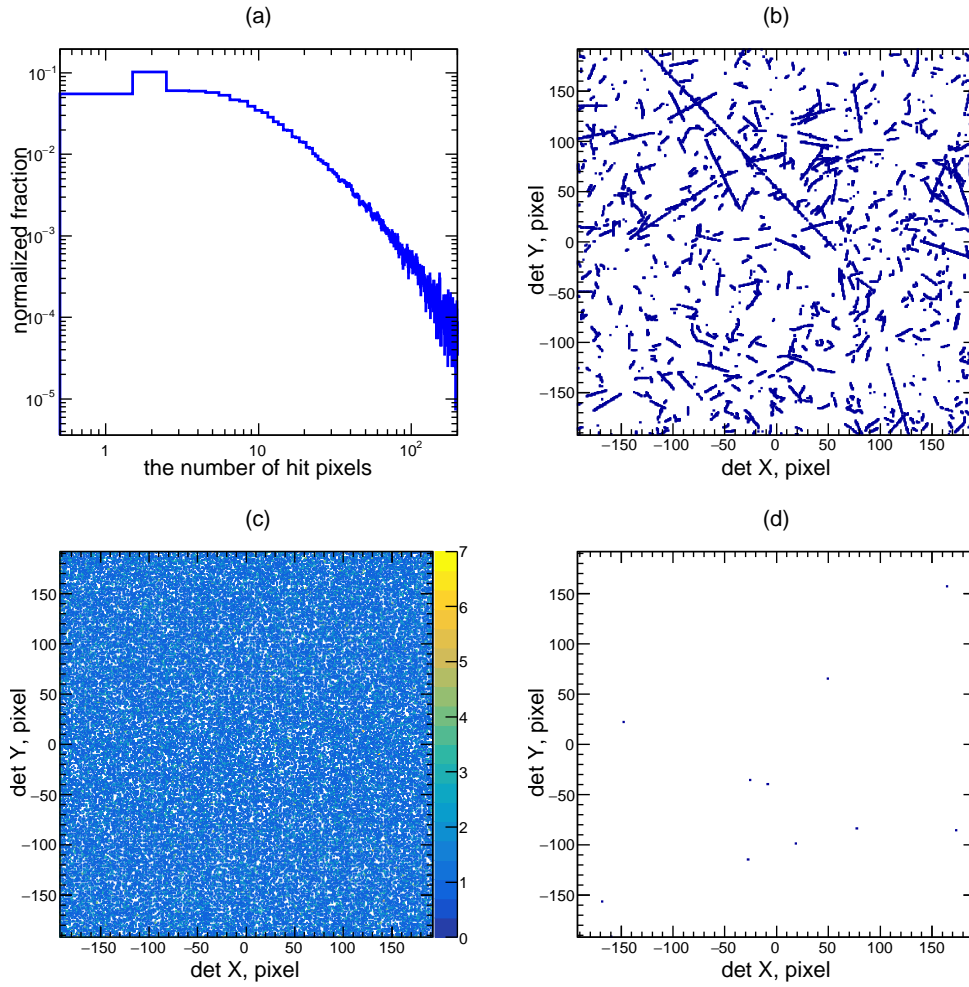


Figure 14: The characteristic of instrumental background induced by primary cosmic ray protons. Each panel plots the same result as Figure 12, except that (b) is the tracks about 122 seconds.

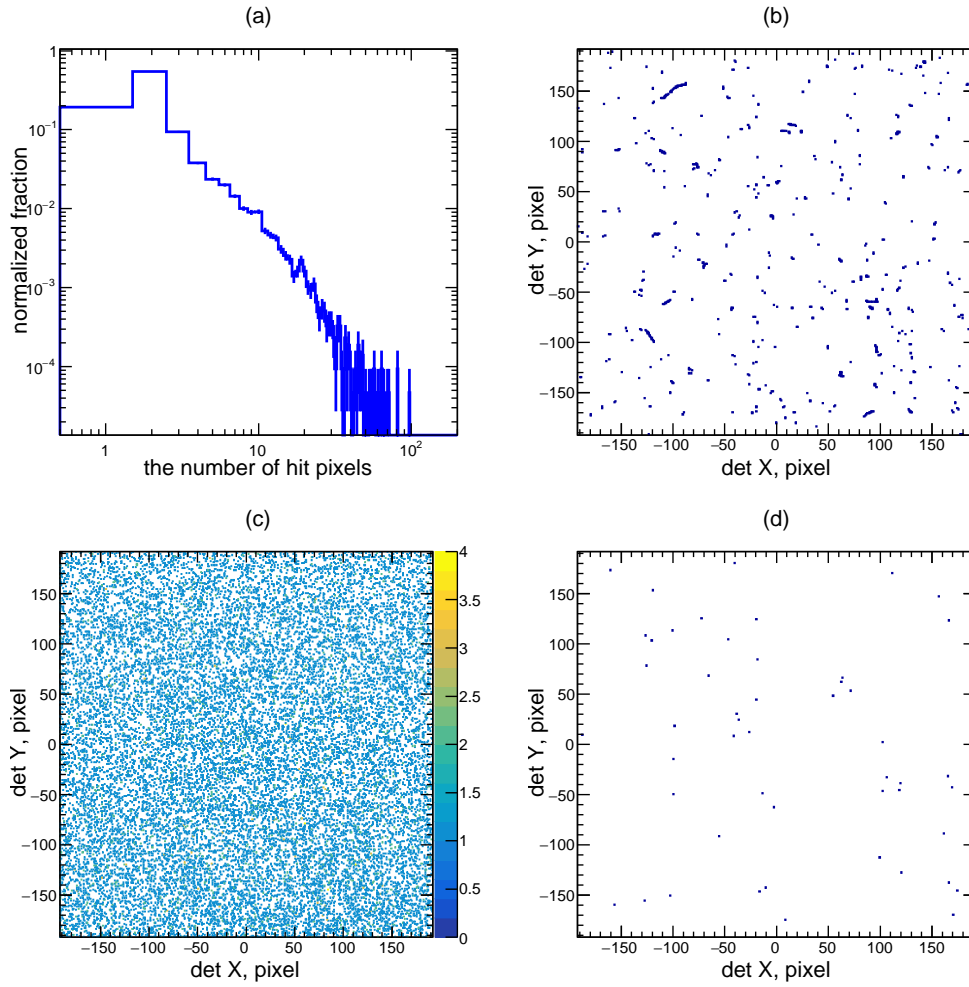


Figure 15: The characteristic of instrumental background induced by cosmic photons. Each panel plots the same result as Figure 12, except that (b) is the tracks about 395 seconds.

and total instrumental background rates on the imaging area of the FPD in different energy bands. The total background spectra for different filter positions are shown in Figure 17. The instrumental background spectrum is obtained by averaging the sum rates of various instrumental background components between 0.5 to 10 keV. It can be seen that the FOV background dominates below ~ 2 keV. Above this energy, the instrumental background is overwhelming. Also plotted in Figure 17 is the observed background spectrum of one eROSITA telescope [42]. For a single telescope, the FOV background of EP/FXT and eROSITA is comparable, while the instrumental background of EP/FXT is about 7 times smaller than that of eROSITA.

Table 2: The background rates of FOV and instrumental background on the imaging area of the FPD and within the focal spot of FXT. The focal spot is taken as a circle with a radius of $30''$ from the center of the optical focus. Unit: counts s^{-1}

on the FPD	0.5-10 keV	0.5-2 keV	2-10 keV
instrument	0.29	0.06	0.23
open	1.61	1.51	0.09
thin	1.27	1.18	0.09
medium	1.00	0.92	0.08
thick	0.46	0.39	0.07
within focal spot	0.5-10 keV	0.5-2 keV	2-10 keV
instrument	5.6×10^{-5}	1.2×10^{-5}	4.4×10^{-5}
open	7.6×10^{-4}	7.0×10^{-4}	5.9×10^{-5}
thin	6.1×10^{-4}	5.5×10^{-4}	6.1×10^{-5}
medium	4.7×10^{-4}	4.2×10^{-4}	5.0×10^{-5}
thick	2.2×10^{-4}	1.8×10^{-4}	4.0×10^{-5}

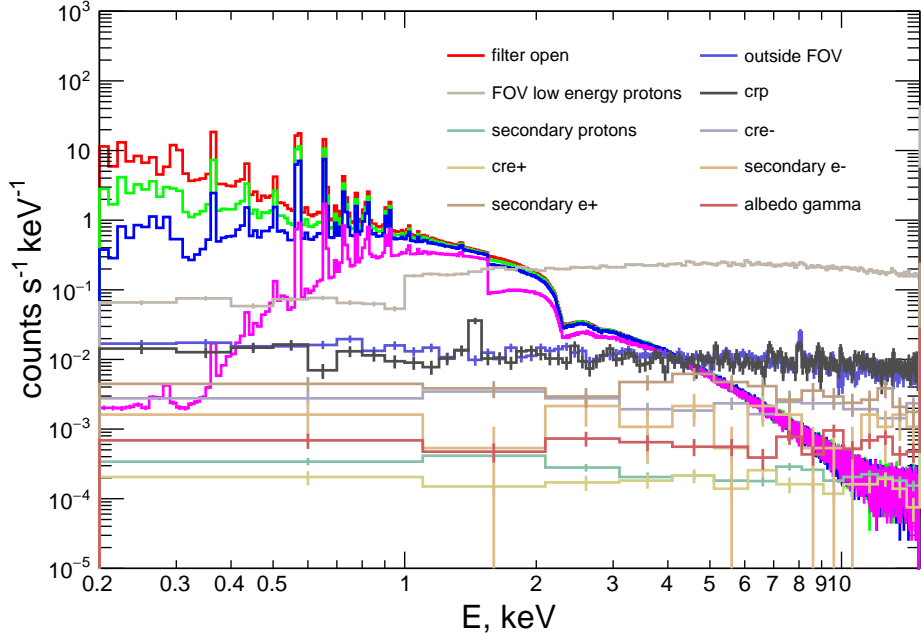


Figure 16: The background spectra caused by various space components on the imaging area of the FPD of FXT. The red (green, blue and magenta) line denotes the FOV background of cosmic photons corresponding to the open (thin, medium and thick) filter position on the filter wheel. The “FOV low energy protons” represents the background induced by the low energy protons near the geomagnetic equator through the funneling effect of the mirrors. For the instrumental background components, the “outside FOV” shows that induced by cosmic photons, “crp” by primary cosmic ray protons, “secondary protons” by secondary cosmic ray protons, “cre-” by primary cosmic ray electrons, “cre+” by primary cosmic ray positrons, “secondary e-” by secondary cosmic ray electrons, “secondary e+” by secondary cosmic positrons and “albedo gamma” by albedo gamma rays.

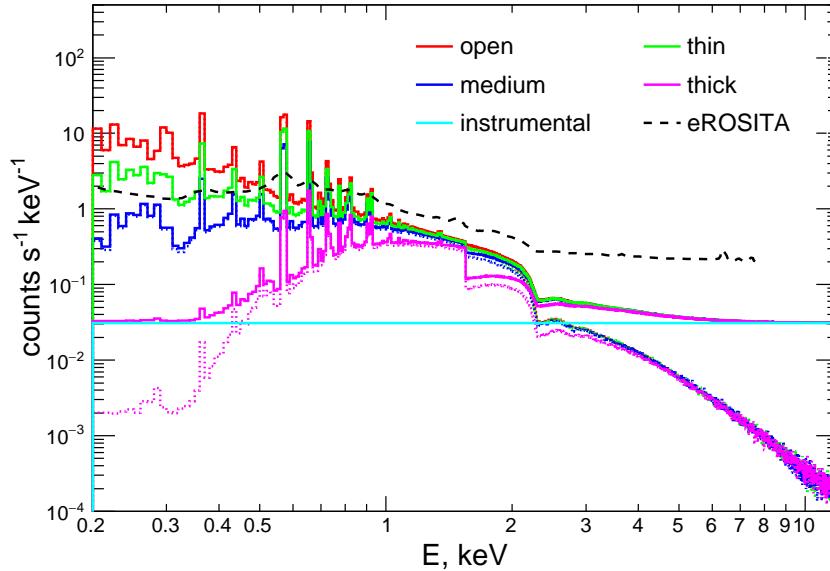


Figure 17: The total background spectra on the imaging area of FXT. The total instrumental background is denoted by the cyan line. The solid (dashed) lines are the total background spectra (FOV background spectra induced by cosmic photons) for different filter wheel positions. The dashed line in black shows the in-orbit background spectrum of one telescope of eROSITA [42].

The general way for an imaging telescope to extract the background to be subtracted from the source signal is to choose a region (the background region) around the source (the source region) on the imaging map. Considering the designed angular resolution of FXT, a circle with a radius of $30''$ is chosen as the source region for the on-axis point sources. This region is also used as the focal spot region in this work. Considering the non uniform distribution of the FOV background on the FPD, the background spectrum extracted from the background region has to be corrected when it is subtracted as the background of the source region. To avoid the systematic error induced by this correction, the background from the source region is extracted to give an estimate of the background level within the focal spot of FXT directly. The FOV and instrumental background rates within the focal spot at different energy bands are listed in Table 2 as well, where the instrumental background is obtained by scaling the instrumental background on the imaging area of the FPD to the focal spot region due to its uniform

distribution on the imaging area, and the FOV background is obtained by counting the events within the focal spot. In the energy band of 0.5-10 keV the instrumental background within the focal spot corresponds to 5.9×10^{-6} counts $\text{s}^{-1} \text{keV}^{-1}$.

5.2. Sensitivity

The sensitivity of EP/FXT could be estimated based on the simulated background. Here the sensitivity is defined as the flux limit of a weak source which can be detected at the 5σ significance level. There are several ways to calculate the detection significance of a source in high energy astrophysics measurements, for example the commonly used Li&Ma method [43] and the specific methods taking into account the impact of different kinds of background uncertainties [44]. In this work, the ideal case [44] where no background uncertainty is adopted. This corresponds to the best theoretical sensitivity limit. And the likelihood ratio method of Li&Ma method [43] are also utilized to have a comparison. For the ideal case, the expected counts from the source is [44]

$$M = 11.090 + 7.415 \times \sqrt{B} \quad (6)$$

for the detection efficiency of 99% at 5σ level, where M is the source counts and B the background counts. Based on the simulated background rate within the focal spot, the sensitivity of FXT is given in Figure 18. It can be seen that, by assuming a Crab-like source spectrum, for once typical pointing observation during EP survey, i.e. an exposure of 25 minutes, the sensitivity of FXT for different filter setup could achieve a level of $(5.9 \sim 11.3) \times 10^{-14}$ $\text{erg cm}^{-2} \text{s}^{-1}$ ($5.1 \sim 9.7 \mu\text{crab}$) in the soft energy band 0.5-2 keV and $(5.9 \sim 7.9) \times 10^{-13}$ $\text{erg cm}^{-2} \text{s}^{-1}$ ($28.0 \sim 37.1 \mu\text{crab}$) in the hard energy band 2-10 keV.

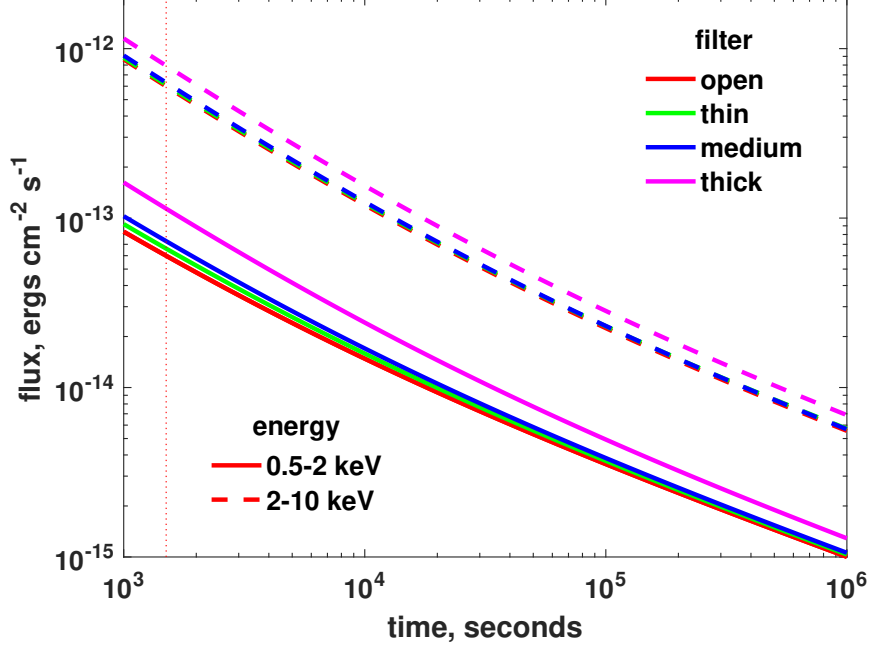


Figure 18: The sensitivity of FXT derived from the ideal case where no background uncertainty is considered [44]. Different line types correspond to different energy bands (solid: 0.5-2 keV; dashed: 2-10 keV). Different line colors denote different filter wheel positions (red: open; green: thin; blue: medium; magenta: thick). Sensitivity is computed for an assumed Crab spectrum, i.e. an absorbed power-law spectrum with an index of 2.05 and a column density $N_{\text{H}}=2 \times 10^{21} \text{ cm}^{-2}$. The vertical dotted line marks the typical exposure time during EP survey, i.e. 1500 seconds.

For the likelihood ratio method, the significance [43]

$$S = \sqrt{2 \times \left\{ M \ln \left[\frac{1 + \alpha}{\alpha} \left(\frac{M}{M + B} \right) \right] + B \ln \left[(1 + \alpha) \left(\frac{B}{M + B} \right) \right] \right\}}. \quad (7)$$

For FXT, α is the ratio of the backgrounds between the source region and the background region. For simplicity, we have taken the background from the focal spot, therefore $\alpha = 1$. The calculated flux for a source with the spectral shape the same as Crab to be detected with an exposure of 25 minutes is $(1.2 \sim 2.2) \times 10^{-13} \text{ erg cm}^{-2} \text{ s}^{-1}$ ($10.6 \sim 18.7 \mu\text{crab}$) in the soft energy band (0.5-2 keV) for different filter positions and $(10.3 \sim 13.5) \times 10^{-13} \text{ erg cm}^{-2} \text{ s}^{-1}$ ($48.5 \sim 64 \mu\text{crab}$) in the hard energy band (2-10 keV). These values are

a bit larger than those shown in Figure 18 because the Poisson distribution of the background is included in this method. In addition, given the uneven background distribution of the cosmic photons on the FPD of FXT, more uncertainties will be introduced and the significance will be reduced in the real observation and data analysis procedure if background counts come from model methods. Then higher fluxes are needed to achieve a 5σ threshold. For example, if a 10% systematic uncertainty on the background estimate is considered, the obtained sensitivity for an exposure of 25 minutes is $(1.6 \sim 2.6) \times 10^{-13} \text{ erg cm}^{-2} \text{ s}^{-1}$ ($13.6 \sim 19.9 \mu\text{crab}$) in the soft energy band (0.5-2 keV) for different filter positions and $(11.0 \sim 14.5) \times 10^{-13} \text{ erg cm}^{-2} \text{ s}^{-1}$ ($52 \sim 69 \mu\text{crab}$) in the hard energy band (2-10 keV).

The sensitivity also depends on the sky area and the spectral characteristics of the source [45]. The Galactic Soft X-ray Background and the Galactic hydrogen column density (N_{H}) vary with the observational pointing direction. To investigate the impact on the sensitivity, we obtained the Soft X-ray Background at the direction of Galactic center, Galactic pole and the lockman hole using the X-ray Background Tool from the HEASARC website⁶, and also got Galactic N_{H} there. Compared with the soft X-ray diffuse background we used in the simulation, the Soft X-ray Background at 0.5-2 keV needs to be scale by a factor of 1.18, 1.22 and 0.53, respectively for the Galactic center, Galactic pole and the lockman hole direction. For the intrinsic spectrum of the target source, two black body spectra with temperatures of 70 eV and 450 eV, respectively and two power-law spectra with indices of 1.7 and 2.05, respectively were considered. The obtained sensitivities in the energy band of 0.5-2 keV are plotted in Figure 19 for these three directions and four spectral shapes. The best result is obtained at the lockman hole direction. The sensitivity with an exposure of 25 minutes varies from $2.9 \times 10^{-14} \text{ erg cm}^{-2} \text{ s}^{-1}$ to $8.7 \times 10^{-14} \text{ erg cm}^{-2} \text{ s}^{-1}$. Compared with the point source sensitivity of the 7 telescopes of eROSITA [42], which is $1.1 \times 10^{-14} \text{ erg cm}^{-2} \text{ s}^{-1}$ in 0.2-2.3 keV, the estimated sensitivity of one FXT module is reasonable in this work.

⁶<https://heasarc.gsfc.nasa.gov/cgi-bin/Tools/xraybg/xraybg.pl>

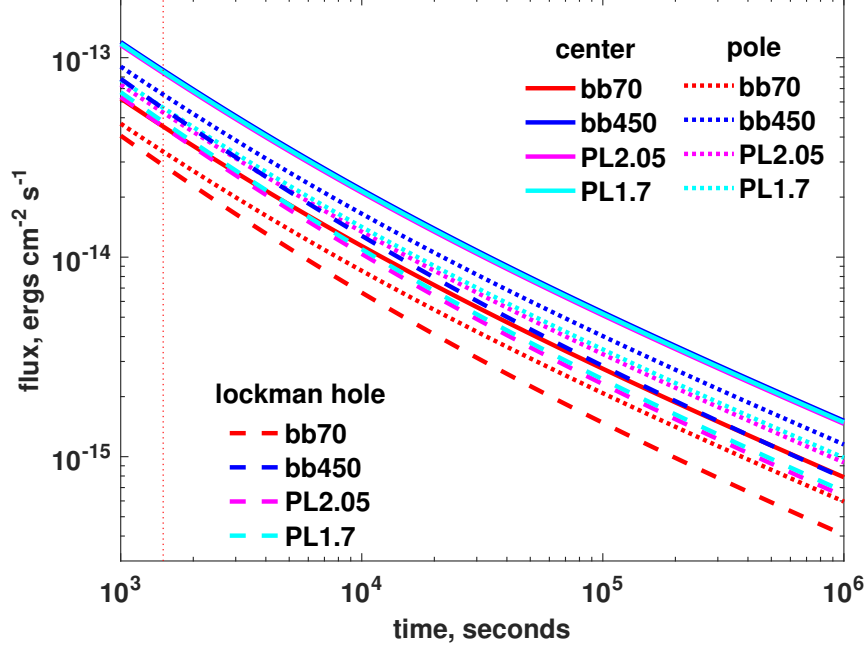


Figure 19: The sensitivity of FXT for different pointing directions and source spectra derived from the ideal case. All the sensitivities plotted here are obtained for the energy band of 0.5-2 keV when the filter wheel is set to open position. Solid lines correspond to the Galactic center pointing direction with a column density $N_{\text{H}} \sim 10^{22} \text{ cm}^{-2}$, dotted lines Galactic pole with $N_{\text{H}} \sim 10^{20} \text{ cm}^{-2}$, and dashed lines the lockman hole with $N_{\text{H}} \sim 5 \times 10^{19} \text{ cm}^{-2}$. Red lines indicate the black body spectrum with a temperature of 70 eV, blue lines the black body spectrum with a temperature of 450 eV, magenta lines the power-law spectrum with an index of 2.05 and cyan lines the power-law spectrum with an index of 1.7. The vertical dotted line marks an exposure of 1500 seconds.

6. Conclusions

In this work, we have obtained an estimate of the in-orbit background of EP/FXT based on simulations using the Geant4 toolkit. We have also given an estimate of its sensitivity based on the obtained background level. During simulation, the energy deposition on the imaging area of the FPD is recorded. For the space radiation environment, the diffuse photon background including the extra-galactic background and the Galactic foreground, the cosmic ray protons, electrons and positrons, as well as the albedo gamma rays and the low-energy protons near the magnetic equator are all consid-

ered. Events that deposited energies on more than three pixels are discarded. The background induced by the equatorial low-energy protons is about one order of magnitude higher than the instrumental background, but it is easily shielded or removed during data analysis and processing. The estimated background level and sensitivity presented in this paper are obtained without the contribution of this component. The instrumental background distributes uniformly on the FPD, and its background level is about 3.1×10^{-2} counts $s^{-1} \text{keV}^{-1}$ (3.7×10^{-3} counts $s^{-1} \text{keV}^{-1} \text{cm}^{-2}$) on the whole imaging area of the FPD and 5.6×10^{-5} counts $s^{-1} \text{keV}^{-1}$ within the focal spot with a radius of $30''$. The FOV background caused by cosmic photons dominates below $\sim 2 \text{keV}$, and the distribution is more concentrated towards the FOV center. Its background rate between 0.5-10 keV is 1.61 counts s^{-1} on the whole FPD and 7.6×10^{-4} counts s^{-1} within the focal spot when the filter wheel is set to the open position. While this rate reduces to 0.46 counts s^{-1} on the whole FPD and 2.2×10^{-4} counts s^{-1} within the focal spot when the filter wheel is set to the thick position. Based on the background level within the focal spot and assuming a Crab-like source spectrum, the estimated ideal sensitivity of FXT could achieve $(5.9 \sim 11.3) \times 10^{-14}$ erg $\text{cm}^{-2} \text{s}^{-1}$ for an exposure of 25 minutes in the energy band of 0.5-2 keV, and $(5.9 \sim 7.9) \times 10^{-14}$ erg $\text{cm}^{-2} \text{s}^{-1}$ in the energy band of 2-10 keV, when the filter wheel is set from open to thick position. If the uncertainty from Poisson distribution is considered, the sensitivity becomes $(1.2 \sim 2.2) \times 10^{-13}$ erg $\text{cm}^{-2} \text{s}^{-1}$ in 0.5-2 keV and $(10.3 \sim 13.5) \times 10^{-13}$ erg $\text{cm}^{-2} \text{s}^{-1}$ in 2-10 keV. Furthermore, if an additional 10% uncertainty from the background subtraction is included, the sensitivity becomes $(1.6 \sim 2.6) \times 10^{-13}$ erg $\text{cm}^{-2} \text{s}^{-1}$ in 0.5-2 keV and $(11.0 \sim 14.5) \times 10^{-13}$ erg $\text{cm}^{-2} \text{s}^{-1}$ in 2-10 keV, about 2 times worse than the idea case.

For the estimated background, it is worth noting that the result given in this work is obtained by adopting the averaged space environment radiation models and zenith satellite pointing attitude. The instrumental background induced by cosmic rays could vary by a factor of ~ 3 from low geomagnetic latitudes to high latitudes according to the background observation of Insight-HXMT [46]. The response of FXT, e.g. the ancillary response file, the point spread function and the vignetting function, are not calibrated due to the lack of ground experimental data currently. Therefore, the FOV background might sort of differ from the real measurement after the launch, and it also varies with the pointing direction in the sky. The soft X-ray background below 2 keV varies by a factor of ~ 2 from the lockman hole direction to

the Galactic center direction according to the ROSAT All-Sky Survey diffuse background maps. The sensitivity not only changes with the background and uncertainty, but also with the pointing direction and the source spectrum. Beside the Crab-like spectrum of a power-law shape with an index of 2.05, we also estimate the sensitivity by assuming a softer power-law spectrum with the index of 1.7 and two black-body spectra with the temperature of 70 eV and 450 eV, respectively. The obtained theoretical sensitivity varies from 2.9×10^{-14} erg cm⁻² s⁻¹ to 8.7×10^{-14} erg cm⁻² s⁻¹ in the energy band of 0.5-2 keV for these four spectra at different pointing directions when the open filter wheel position is set. The estimated in-orbit background level and sensitivity of FXT in this work will help conduct the observation simulation, make up the observation strategy and pre-study the scientific targets.

Declaration of Competing Interest

The authors declare that they have no known competing financial interests or personal relationships that could have appeared to influence the work reported in this paper.

Acknowledgements

We are grateful to all the colleagues in EP team. J. Zhang thank Z. C. Tang for the discussion with AMS-02 data. This work is supported by the Einstein-Probe (EP) Program which is funded by the Strategic Priority Research Program of the Chinese Academy of Sciences Grant No.XDA15310000. We also acknowledge Project 12003037 supported by the National Natural Science Foundation of China.

References

- [1] W. Yuan, C. Zhang, Z. Ling, et al., Einstein Probe: a lobster-eye telescope for monitoring the x-ray sky, in: J.-W. A. den Herder, S. Nikzad, K. Nakazawa (Eds.), *Space Telescopes and Instrumentation 2018: Ultraviolet to Gamma Ray*, Vol. 10699 of Society of Photo-Optical Instrumentation Engineers (SPIE) Conference Series, 2018, p. 1069925. doi:10.1117/12.2313358.

- [2] W. Yuan, L. Amati, J. K. Cannizzo, et al., Perspectives on Gamma-Ray Burst Physics and Cosmology with Next Generation Facilities, *Space Sci. Rev.*202 (1-4) (2016) 235–277. [arXiv:1606.09536](#), [doi:10.1007/s11214-016-0274-z](#).
- [3] W. Yuan, C. Zhang, Y. Chen, et al., Einstein Probe: Exploring the ever-changing X-ray Universe, *Scientia Sinica Physica, Mechanica & Astronomica* 48 (3) (2018) 039502. [doi:10.1360/SSPMA2017-00297](#).
- [4] D. Zhao, C. Zhang, W. Yuan, et al., Geant4 simulations of a wide-angle x-ray focusing telescope, *Experimental Astronomy* 43 (3) (2017) 267–283. [arXiv:1703.09380](#), [doi:10.1007/s10686-017-9534-5](#).
- [5] C. Tenzer, G. Warth, E. Kendziorra, A. Santangelo, Geant4 simulation studies of the eROSITA detector background, in: A. D. Holland, D. A. Dorn (Eds.), *High Energy, Optical, and Infrared Detectors for Astronomy IV*, Vol. 7742 of Society of Photo-Optical Instrumentation Engineers (SPIE) Conference Series, 2010, p. 77420Y. [doi:10.1117/12.857087](#).
- [6] E. Perinati, C. Tenzer, A. Santangelo, et al., The radiation environment in L-2 orbit: implications on the non-X-ray background of the eROSITA pn-CCD cameras, *Experimental Astronomy* 33 (1) (2012) 39–53. [doi:10.1007/s10686-011-9269-7](#).
- [7] G. Weidenspointner, M. G. Pia, A. Zoglauer, Application of the Geant4 PIXE implementation for space missions new models for PIXE simulation with Geant4, in: *2008 IEEE Nuclear Science Symposium and Medical Imaging Conference and 16th International Workshop on Room-Temperature Semiconductor X-Ray and Gamma-Ray Detectors*, 2008, p. 2877–2884. [doi:10.1109/NSSMIC.2008.4774969](#).
- [8] V. Fioretti, A. Bulgarelli, G. Malaguti, et al., Monte Carlo simulations of soft proton flares: testing the physics with XMM-Newton, in: J.-W. A. den Herder, T. Takahashi, M. Bautz (Eds.), *Space Telescopes and Instrumentation 2016: Ultraviolet to Gamma Ray*, Vol. 9905 of Society of Photo-Optical Instrumentation Engineers (SPIE) Conference Series, 2016, p. 99056W. [arXiv:1607.05319](#), [doi:10.1117/12.2232537](#).

- [9] R. Campana, M. Feroci, E. Del Monte, et al., Background simulations for the Large Area Detector onboard LOFT, *Experimental Astronomy* 36 (3) (2013) 451–477. [arXiv:1305.3789](#), [doi:10.1007/s10686-013-9341-6](#).
- [10] F. Xie, M. Pearce, A Study of Background Conditions for Sphinx—The Satellite-Borne Gamma-Ray Burst Polarimeter, *Galaxies* 6 (2) (2018) 50. [arXiv:1809.06629](#), [doi:10.3390/galaxies6020050](#).
- [11] F. Xie, J. Zhang, L.-M. Song, et al., Simulation of the in-flight background for HXMT/HE, *Ap&SS*360 (2015) 13. [arXiv:1511.02997](#), [doi:10.1007/s10509-015-2559-1](#).
- [12] J. Zhang, X. Li, M. Ge, et al., Comparison of simulated backgrounds with in-orbit observations for HE, ME, and LE onboard Insight-HXMT, *Ap&SS*365 (9) (2020) 158. [arXiv:2009.14489](#), [doi:10.1007/s10509-020-03873-8](#).
- [13] S. Agostinelli, et al., GEANT4—a simulation toolkit, *Nucl. Instrum. Meth. A* 506 (2003) 250–303. [doi:10.1016/S0168-9002\(03\)01368-8](#).
- [14] J. Allison, et al., Geant4 developments and applications, *IEEE Trans. Nucl. Sci.* 53 (2006) 270. [doi:10.1109/TNS.2006.869826](#).
- [15] J. Allison, et al., Recent developments in Geant4, *Nucl. Instrum. Meth. A* 835 (2016) 186–225. [doi:10.1016/j.nima.2016.06.125](#).
- [16] E. J. Buis, G. Vacanti, X-ray tracing using Geant4, *Nuclear Instruments and Methods in Physics Research A* 599 (2-3) (2009) 260–263. [arXiv:0810.1273](#), [doi:10.1016/j.nima.2008.11.002](#).
- [17] L. Q. Qi, G. Li, Y. P. Xu, et al., Geant4 simulation for the responses to X-rays and charged particles through the eXTP focusing mirrors, *Nuclear Instruments and Methods in Physics Research A* 963 (2020) 163702. [doi:10.1016/j.nima.2020.163702](#).
- [18] V. S. Remizovich, M. I. Ryazanov, I. S. Tilinin, Energy and angular distributions of particles reflected in glancing incidence of a beam of ions on the surface of a material, *Soviet Journal of Experimental and Theoretical Physics* 52 (1980) 225.

- [19] R. Amato, T. Mineo, A. D’Ai, et al., Soft proton scattering at grazing incidence from X-ray mirrors: analysis of experimental data in the framework of the non-elastic approximation, *Experimental Astronomy* 49 (3) (2020) 115–140. [arXiv:2003.07295](#), [doi:10.1007/s10686-020-09657-w](#).
- [20] A. Guzmán, E. Perinati, S. Diebold, et al., A revision of soft proton scattering at grazing incidence and its implementation in the geant4 toolkit, *Experimental Astronomy* 44 (3) (2017) 401–411. [doi:10.1007/s10686-017-9537-2](#).
- [21] N. Gehrels, Instrumental background in gamma-ray spectrometers flown in low Earth orbit, *Nuclear Instruments and Methods in Physics Research A* 313 (3) (1992) 513–528. [doi:10.1016/0168-9002\(92\)90832-0](#).
- [22] D. E. Gruber, J. L. Matteson, L. E. Peterson, G. V. Jung, The Spectrum of Diffuse Cosmic Hard X-Rays Measured with HEAO 1, *ApJ*520 (1) (1999) 124–129. [arXiv:astro-ph/9903492](#), [doi:10.1086/307450](#).
- [23] D. McCammon, R. Almy, E. Apodaca, et al., A High Spectral Resolution Observation of the Soft X-Ray Diffuse Background with Thermal Detectors, *ApJ*576 (1) (2002) 188–203. [arXiv:astro-ph/0205012](#), [doi:10.1086/341727](#).
- [24] <https://www.mpe.mpg.de/ATHENA-WFI/public/resources/background/WFI-MPE-ANA-Background-20150327.pdf>.
- [25] L. J. Gleeson, W. I. Axford, Solar Modulation of Galactic Cosmic Rays, *ApJ*154 (1968) 1011. [doi:10.1086/149822](#).
- [26] E. Frigo, F. Antonelli, D. S. S. da Silva, et al., Effects of solar activity and galactic cosmic ray cycles on the modulation of the annual average temperature at two sites in southern Brazil, *Annales Geophysicae* 36 (2) (2018) 555–564. [doi:10.5194/angeo-36-555-2018](#).
- [27] T. Mizuno, T. Kamae, G. Godfrey, et al., Cosmic-Ray Background Flux Model Based on a Gamma-Ray Large Area Space Telescope Balloon Flight Engineering Model, *ApJ*614 (2) (2004) 1113–1123. [arXiv:astro-ph/0406684](#), [doi:10.1086/423801](#).

- [28] J. Alcaraz, et al., Protons in near earth orbit, *Phys. Lett. B* 472 (2000) 215–226. [arXiv:hep-ex/0002049](#), [doi:10.1016/S0370-2693\(99\)01427-6](#).
- [29] J. Alcaraz, et al., Cosmic protons, *Phys. Lett. B* 490 (2000) 27–35. [doi:10.1016/S0370-2693\(00\)00970-9](#).
- [30] M. Aguilar, et al., Precision Measurement of the Proton Flux in Primary Cosmic Rays from Rigidity 1 GV to 1.8 TV with the Alpha Magnetic Spectrometer on the International Space Station, *Phys. Rev. Lett.* 114 (2015) 171103. [doi:10.1103/PhysRevLett.114.171103](#).
- [31] J. Moritz, Energetic protons at low equatorial altitudes., *Zeitschrift fur Geophysik* 38 (1972) 701–717.
- [32] A. N. Petrov, O. R. Grigoryan, M. I. Panasyuk, Energy spectrum of proton flux near geomagnetic equator at low altitudes, *Advances in Space Research* 41 (8) (2008) 1269–1273. [doi:10.1016/j.asr.2007.08.007](#).
- [33] A. N. Petrov, O. R. Grigoryan, N. V. Kuznetsov, Creation of model of quasi-trapped proton fluxes below Earth’s radiation belt, *Advances in Space Research* 43 (4) (2009) 654–658. [doi:10.1016/j.asr.2008.11.019](#).
- [34] E. Kendziorra, T. Clauss, N. Meidinger, et al., Effect of low-energy protons on the performance of the EPIC pn-CCD detector on XMM-Newton, in: K. A. Flanagan, O. H. Siegmund (Eds.), *X-Ray and Gamma-Ray Instrumentation for Astronomy XI*, Vol. 4140 of Society of Photo-Optical Instrumentation Engineers (SPIE) Conference Series, 2000, p. 32–41. [doi:10.1117/12.409132](#).
- [35] D. H. Lo, J. R. Srour, Modeling of proton-induced ccd degradation in the chandra x-ray observatory, *IEEE Transactions on Nuclear Science* 50 (6) (2003) 2018–2023. [doi:10.1109/TNS.2003.820735](#).
- [36] L. Qi, G. Li, Y. Xu, et al., A preliminary design of the magnetic diverter on-board the eXTP observatory, *Experimental Astronomy* (Mar. 2021). [doi:10.1007/s10686-021-09707-x](#).
- [37] M. Aguilar, D. Aisa, A. Alvino, et al., Electron and Positron Fluxes in Primary Cosmic Rays Measured with the Alpha Magnetic Spectrometer

- on the International Space Station, *Phys. Rev. Lett.* 113 (12) (2014) 121102. doi:10.1103/PhysRevLett.113.121102.
- [38] M. Aguilar, L. Ali Cavazonza, B. Alpat, et al., Towards Understanding the Origin of Cosmic-Ray Electrons, *Phys. Rev. Lett.* 122 (10) (2019) 101101. doi:10.1103/PhysRevLett.122.101101.
- [39] R. L. Golden, C. Grimani, B. L. Kimbell, et al., Observations of Cosmic-Ray Electrons and Positrons Using an Imaging Calorimeter, *ApJ* 436 (1994) 769. doi:10.1086/174951.
- [40] O. R. Grigoryan, M. I. Panasyuk, V. L. Petrov, et al., Spectral characteristics of electron fluxes at $L < 2$ under the Radiation Belts, *Advances in Space Research* 42 (9) (2008) 1523–1526. doi:10.1016/j.asr.2007.12.009.
- [41] S. Granato, R. Andritschke, J. Elbs, et al., Characterization of eROSITA PNCCDs, *IEEE Transactions on Nuclear Science* 60 (4) (2013) 3150–3157. doi:10.1109/TNS.2013.2269907.
- [42] P. Predehl, R. Andritschke, V. Arefiev, et al., The eROSITA X-ray telescope on SRG, *A&A* 647 (2021) A1. arXiv:2010.03477, doi:10.1051/0004-6361/202039313.
- [43] T. P. Li, Y. Q. Ma, Analysis methods for results in gamma-ray astronomy., *ApJ* 272 (1983) 317–324. doi:10.1086/161295.
- [44] G. Vianello, The Significance of an Excess in a Counting Experiment: Assessing the Impact of Systematic Uncertainties and the Case with a Gaussian Background, *ApJS* 236 (1) (2018) 17. arXiv:1712.00118, doi:10.3847/1538-4365/aab780.
- [45] "XMM-Newton Users Handbook", Issue 2.17, 2019 (ESA: XMM-Newton SOC).
- [46] J.-Y. Liao, S. Zhang, Y. Chen, et al., Background model for the Low-Energy Telescope of Insight-HXMT, *Journal of High Energy Astrophysics* 27 (2020) 24–32. arXiv:2004.01432, doi:10.1016/j.jheap.2020.02.010.